HIGH POWER LASER
SCIENCE AND ENGINEERING

RESEARCH ARTICLE

Diode-pumped high-power continuous-wave intracavity frequency-doubled Pr^{3+}:YLF ultraviolet lasers around 349 nm

Xiuji Lin, Zheng Zhang, Shuaihao Ji, Run Fang, Bo Xiao, Huiying Xu, and Zhiping Cai[iD]

Department of Electronic Engineering, Xiamen University, Xiamen, China
(Received 23 August 2022; revised 30 September 2022; accepted 25 October 2022)

Abstract

High-power continuous-wave ultraviolet lasers are useful for many applications. As ultraviolet laser sources, the wavelength switching capability and compact structure are very important to extend the applicability and improve the flexibility in practical applications. In this work, we present two simple and relatively compact schemes by laser diode pumping to obtain a watt-level single-wavelength 348.7-nm laser and discrete wavelength tunable ultraviolet lasers around 349 nm (from 334.7 to 364.5 nm) by intracavity frequency doubling based on Pr^{3+}:YLF and β-BBO crystals. The maximum output power of the single-wavelength 348.7-nm laser is 1.033 W. The output powers of the discrete wavelength tunable lasers are at the level of tens of milliwatts, except for two peaks at 348.7 and 360.3 nm with output powers of approximately 500 mW. In addition, simulations are carried out to explain the experimental results and clarify the tuning mechanisms.

Keywords: high-power ultraviolet laser; Pr^{3+}:YLF; tunable ultraviolet laser
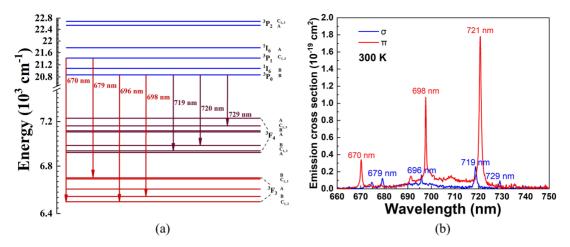
1. Introduction

High-power continuous-wave (CW) ultraviolet (UV) lasers are required in plentiful applications, including metal welding, material processing, Raman spectroscopy, flow cytometry, photothermal detection and biomedical applications[1–6]. There are some approaches to obtain high-power UV lasers (e.g., sum-frequency generation (SFG) lasers based on Nd^{3+} doped materials, excimer lasers, argon ion lasers, nitrogen lasers and free electron lasers[7–11]) and tunable UV lasers (e.g., intracavity tripled Ti:sapphire lasers, optical parametric oscillators, intracavity frequency tripling semiconductor lasers, UV lasers based on Ce^{3+} doped materials, Ar-filled photonic crystal fiber lasers, second-harmonic generation (SHG) dye lasers and SFG lasers based on Nd^{3+} doped materials[12–17]). However, some of them have difficulties in CW operations or obtaining high output powers, and most of them are complex, expensive and bulky.

As is well known, the Pr^{3+}:YLF crystal has been proved to exhibit excellent laser performance in the visible region[18–27]. Thanks to the development of the blue laser

diode (LD), it is easier to realize more compact high-power LD-pumped Pr^{3+}:YLF lasers[28,29]. Due to the outstanding visible laser performance, it is natural that people start to build more compact UV laser sources based on the Pr^{3+}:YLF crystal through SHG[30–36]. Although there are many previous works that achieve UV lasers based on Pr^{3+}:YLF and nonlinear crystals, the laser output powers at approximately 349 nm are still very low (~33 mW[37]) and the spectral resources of the Pr^{3+}:YLF crystal in the deep red region have evidently not been fully developed to realize tunable UV laser sources. To show the potential of realizing tunable deep red laser frequency doubling by the Pr^{3+}:YLF crystal, we present major laser transitions from related fine energy-level structures ($^3P_{0,1,2}$ to $^3F_4$, $^3F_3$) and emission cross-sections in the deep red region of the Pr^{3+}:YLF crystal (see Figure 1).

According to the current situations and reasons mentioned above, we realize a watt-level UV laser at 348.7 nm and discrete tunable UV lasers from 334.7 to 364.5 nm. The lasers are achieved by intracavity frequency-doubled schemes based on Pr^{3+}:YLF and β-BBO crystals. The wavelength tunability is achieved by rotating an intracavity Lyot filter and tilting the β-BBO crystal. The maximum output power of the laser at 348.7 nm generated through the

Correspondence to: Zhiping Cai, Department of Electronic Engineering, Xiamen University, Xiamen 361005, China. Email: zpcai@xmu.edu.cn

1

Figure 1. Some spectroscopy properties of the Pr^{3+}:YLF crystal. (a) Major deep red laser transitions of the Pr^{3+}:YLF crystal from $^3P_{0,1,2}$ to $^3F_4$, $^3F_3$[38]. (b) Emission cross-sections of the Pr^{3+}:YLF crystal in the deep red region.

fundamental laser at approximately 698 nm is 1.033 W. The M^2 factors are measured to be 2.0 and 2.8 in the horizontal (*x*) and vertical (*y*) directions, respectively. The discrete wavelength tunable lasers have output powers of tens of milliwatts, excluding two peaks at 348.7 and 360.3 nm, with approximately 500 mW output powers. Theoretical simulations are also carried out to interpret the tuning mechanisms during the combination of the β-BBO crystal and the birefringent filter. To the best of our knowledge, the output power of the 348.7-nm laser is the highest, and a discrete tunable UV laser based on the Pr^{3+}:YLF crystal is realized for the first time. The results we obtained show that our approaches have enormous potential to be cheaper, simpler and more compact competitors as compared with frequently used high-power CW UV laser sources in practical applications.

2. Experimental details

To obtain high-power CW UV lasers at 348.7 nm, an *a*-cut Pr^{3+}:YLF crystal (uncoated) and a β-BBO crystal (antireflective (AR) coated at ~349 and ~698 nm) were used in the experiment. The concentration of the Pr^{3+}:YLF crystal is approximately 0.12% (atomic fraction). The length of the Pr^{3+}:YLF crystal is 15 mm, and the crystal is a square rod with 3 mm × 3 mm polished windows on two sides. The Pr^{3+}:YLF crystal was mounted in a water cooled copper block and wrapped with indium foil to keep it working under a relatively low temperature (3°C) to reduce the thermal lensing effects and the probability of thermal fragmentation. The β-BBO crystal is a square rod with 7-mm length and two 4 mm × 4 mm coated end faces. The β-BBO crystal was also wrapped with indium foil and clamped in a copper block. The copper block for the β-BBO crystal is without water cooling since the crystal has a very large phase-matching temperature[39]. The β-BBO crystal was cut for type-I phase matching and designed for frequency doubling of a normally incident 698-nm laser beam (the

phase-matching angle is 33.8°). A 24-W commercial LD array emitting at approximately 444 nm (peak wavelength under maximum output power) with a collimated output laser beam was utilized in the experiment as the LD pump source. The M^2 factors of the LD array are 46.9 and 15.5 in the *x* and *y* directions (calculated through the parameters provided by the manufacturer), respectively. The beam diameters at the output port (beam waist) of the LDs are 5.2 and 3.8 mm in the horizontal and vertical directions, respectively. The maximum pump absorption efficiency of the Pr^{3+}:YLF crystal is approximately 51%. The linewidth of the LD array is relatively large (2.2 nm). The experimental schemes are presented in Figure 2(a). There are some differences between the schemes to obtain a high-power single-wavelength laser at 348.7 nm and discrete tunable UV lasers: the Lyot filter was only inserted into the cavity for the discrete tunable UV lasers, the focal lengths of the focusing lenses were different, the cavity lengths were slightly different and the plane mirrors close to the β-BBO crystal were different. As seen in Figure 2(a), plano-convex lenses with 100- and 75-mm focal lengths were applied as focusing lenses to obtain a high-power single-wavelength laser at 348.7 nm and discrete tunable UV lasers, respectively. In order to get a high output power at 348.7 nm, a focusing lens with a longer focal length was applied to reduce the thermal lensing effects. On the other hand, to obtain more wavelengths, a focusing lens with a shorter focal length was utilized to reduce the deep red laser thresholds. The Lyot filter is an *a*-cut quartz crystal with 1-mm thickness, and it was inserted into the laser cavity at the Brewster angle. The insertion directions of the Lyot filter depended on the polarization directions (σ and π) of the fundamental laser. Then, the wavelength tunability could be achieved by rotating the intracavity Lyot filter and tilting the β-BBO crystal. Mirror M1 is a plane mirror with high transmittance in the blue to red region (up to 650 nm) and high reflectivity in the
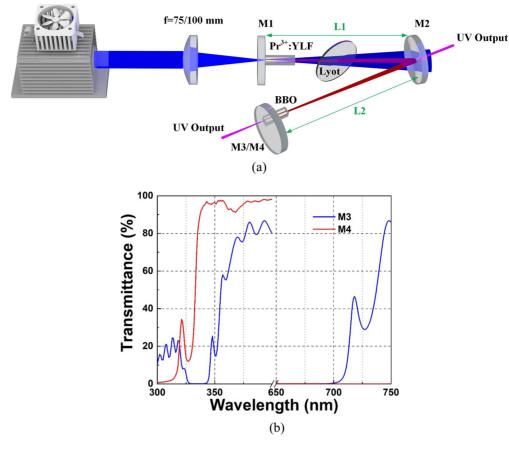
(a)

(b)

Figure 2. (a) Experimental scheme for CW UV lasers. (b) Transmittance curves of the M3 and M4 mirrors.

deep red region. Thus, the unwanted green, orange and red emissions could be suppressed by mirror M1. Mirror M2 is a plane-concave mirror with a radius of curvature of 100 mm and a dielectric coating on the concave surface. Mirror M2 has a high reflectivity in the deep region and relatively high transmittance of around 349 nm (~80%). Therefore, the total output power of the UV laser should be corrected by considering the transmittance of the M2 mirror. Plane mirrors M3 and M4 were applied to obtain a high-power 348.7-nm UV laser and discrete tunable UV lasers, respectively. The reason for using the M3 mirror for the high-power 348.7-nm UV laser was that the relatively high transmittance at 721 nm (~39%) and the high reflectivity at 698 nm of this mirror were required to eliminate the oscillation of the 721-nm laser and store the 698-nm laser power inside the cavity. Mirror M4 was used to obtain discrete tunable UV lasers due to a wide range of high reflectivity in the deep red region. The transmittance curves of the M3 and M4 mirrors are presented in Figure 2(b). The total cavity lengths for the single-wavelength 348.7-nm UV laser and the discrete tunable UV lasers were adjusted to 181 mm (the lengths of the L1 and L2 arms were 89 and 92 mm, respectively) and 193 mm (the lengths of the L1 and L2 arms were 95 and 98 mm, respectively), respectively. Besides, multi-wavelength UV lasers could also be obtained

by the scheme for discrete tunable UV lasers. The related results for multi-wavelength UV lasers are presented in the supplementary material.

3. Results and discussion

3.1. High-power CW single-wavelength UV laser at 348.7 nm

3.1.1. Results
The results of the high-power CW single-wavelength 348.7-nm laser are presented in Figure 3. As seen in Figure 3(a), the total maximum output power of 1.033 W was achieved for the CW single-wavelength UV laser at 348.7 nm. The output power was corrected by the transmittance of the M2 mirror. The optical-to-optical conversion efficiency with respect to the absorbed power could be calculated to be approximately 9.4%. The threshold of the laser was 0.58 W (absorbed pump power). The M^2 factors were measured to be 2.0 and 2.8 in the x and y directions, respectively. Since our LD array could not work for a long enough time under the maximum output power to finish the measurement of the M^2 factors, we measured the M^2 factors under a relatively low pump power with a UV laser power of approximately 0.6 W. The M^2 factors at the
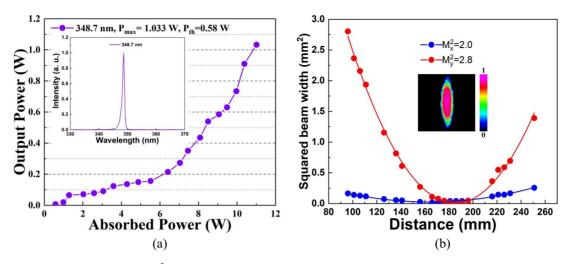
Figure 3. Output powers, laser spectrum and M^2 factors of the high-power CW single-wavelength UV laser at 348.7 nm. (a) Output powers with respect to absorbed pump powers and the laser spectrum. (b) M^2 factors of the 348.7-nm laser beam in the x and y directions.

maximum output power should be a little higher. The highly elliptical UV laser beam profile should be mainly introduced by the relatively large work-off angle of the β-BBO crystal and the relatively strong thermal lensing effects in the π direction of the YLF crystal.
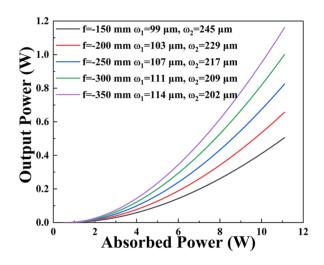
3.1.2. Analyses

Compared with the previous work on 698-nm laser frequency doubling[37], the output power was greatly improved (~31 times). However, the optical-to-optical conversion efficiency was little improved, despite the much higher pump power. To explain the reason, we did some simulations based on the intracavity frequency doubling theory under plane wave approximation proposed by Smith[40] and Agnesi *et al.* [41]:

$$P_{2\omega} = \frac{\pi \omega_1^2}{8k} I_s^2 \left\{ -\left(k + \frac{L_i}{I_s}\right) + \left[\left(k + \frac{L_i}{I_s}\right)^2 + 4\frac{k}{I_s}(2K_c P_a - L_i)\right]^{1/2}\right\}^2,$$ (1)

$$k = \frac{4\pi^2}{\lambda_\omega^2} Z_0 \frac{d_{eff}^2 \ell^2}{n^2} \frac{\omega_1^2}{\omega_2^2} \beta,$$ (2)

where ω_1 and ω_2 are the laser beam sizes in the gain medium and nonlinear crystal, I_s is the saturation intensity of the 698-nm transition, K_c is the coupling efficiency, L_i is the intracavity loss, P_a is the absorbed pump power, $P_{2\omega}$ is the power of the frequency-doubled laser, λ_ω is the wavelength of the fundamental laser, $Z_0 = 337\ \Omega$ is the vacuum impedance, d_{eff} is the nonlinear coefficient of the nonlinear crystal (which also depends on the type of phase matching), ℓ is the length of the nonlinear crystal (7 mm), n is the refractive index of the nonlinear crystal at $\lambda_{2\omega}$ (1.7 in the simulation) and β is the phase mismatching factor (~2 in the simulation). Here, ω_1 and ω_2 were calculated through the well-known ABCD matrix theory by using different effective thermal focal lengths of the gain medium; I_s was calculated to be 5.3×10^8 W/m^2; K_c was evaluated to be approximately 0.043 W^{-1}; L_i was evaluated to be
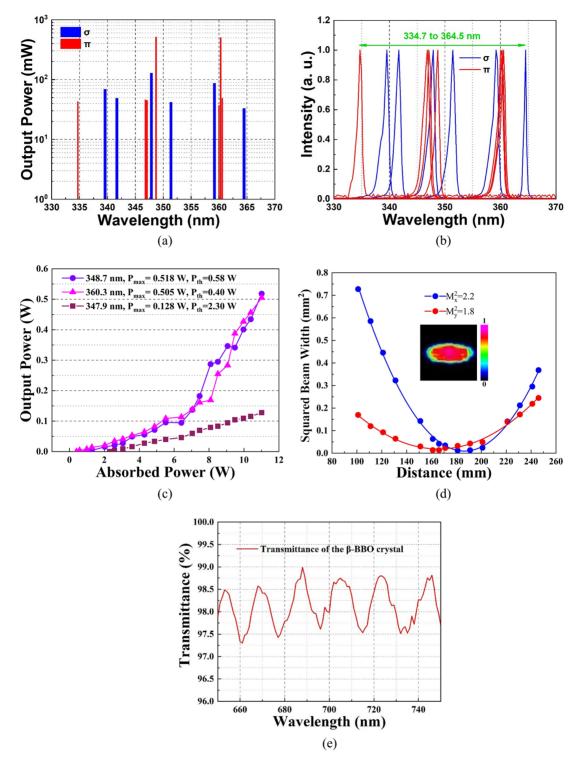

Figure 4. Simulation results of the 348.7-nm laser output powers under different effective thermal focal lengths. Here, f is the value of the effective thermal focal length and ω_1 and ω_2 are the laser beam sizes in the gain medium and nonlinear crystal, respectively.

approximately 0.05 according to the transmission of the β-BBO crystal at 698 nm (~98%); d_{eff} of the β-BBO crystal under type-I phase matching could be obtained through the parameters in Ref. [39]. The simulation results are presented in Figure 4. As seen, the UV laser performances are sensitive to the thermal lensing effects, and the output powers are lower when the thermal lensing effects become stronger. Thus, we can see that the optical-to-optical conversion efficiency was not significantly improved due to the much stronger thermal lensing effects introduced by the higher pump power compared with the previous work[37].

3.2. Discrete tunable CW UV lasers

3.2.1. Results

The measured results of the CW discrete tunable UV lasers are presented in Figure 5. The wavelength tunability was realized by rotating the intracavity Lyot filter and tilting the

Figure 5. Measured results for the CW discrete tunable UV lasers. (a) Laser output powers at different wavelengths. (b) Laser spectra corresponding to (a). (c) Output powers with respect to the absorbed pump powers of the two lasers with relatively high output powers. (d) M^2 factors of the 347.9-nm laser beam in the *x* and *y* directions. (e) The transmittance of the β-BBO crystal (normal incidence) in the deep red region.

β-BBO crystal. As seen in Figure 5(a), lasers at different wavelengths were obtained by wavelength tuning. Most of the output powers achieved were at the level of tens of milliwatts, except for the lasers at 347.8 and 360.3 nm (~500 mW). The fundamental lasers in the σ and π polarization directions were both realized to generate the UV lasers. As seen from Figure 5(b), lasers from 334.7 to 364.6 nm were achieved, including both the σ and π polarization directions. Continuous tunability was only realized in some narrow ranges (from 360.0 to 360.6 nm, and from
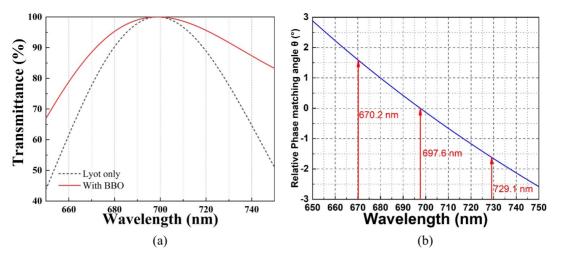
Figure 6. Simulation results to further understand the wavelength tuning. (a) Round trip TM mode transmittances comparison of using only the 1-mm thick quartz plate and both the plate and the β-BBO crystal at the same time. (b) Relative phase-matching angles at different wavelengths of the β-BBO crystal.

347.8 to 349.1 nm). The input–output characteristics of the lasers with relatively high output powers are presented in Figure 5(c). The maximum output powers of the lasers at 348.7 and 360.3 nm were 0.518 and 0.505 W, respectively. The thresholds of the two lasers at 348.7 and 360.3 nm were 0.58 and 0.4 W, respectively. The 347.9-nm laser generated through the σ-polarized fundamental laser had a maximum output power of 128 mW with a threshold of 2.30 W. As seen from Figure 5(d), although the YLF crystal in the scheme for σ-polarized fundamental laser tuning suffered higher waste heat, the M^2 factors of the generated UV laser beam (2.2 and 1.8 in the x and y directions, respectively) were smaller than the aforementioned one generated through the π-polarized fundamental laser. The reason could be that the thermal lensing effects in the π direction of the YLF crystal are stronger than those in the σ direction. The stronger thermal lensing effects could introduce detrimental influences to the beam quality. Due to the slightly stronger thermal lensing effects in this scheme (compared with the single-wavelength scheme) and the higher intracavity losses introduced by the extra Lyot filter due to the laser divergence angle, the output power obtained at 348.7 nm was much lower than that of the laser achieved by the single-wavelength scheme. The 360.3-nm laser output power was expected to be higher than that of the laser at 348.7 nm due to the larger emission cross-section at approximately 721 nm (compared with the emission cross-section at ~698 nm). However, as seen from Figure 5(e), the quality of the AR coating on the β-BBO crystal was not so ideal. When the β-BBO crystal was tilted to the correct phase-matching angle, the transmittance of the crystal at approximately 721 nm might be lower than the normally incident transmittance at approximately 698 nm. The other reason was that when the fundamental laser was normally incident, a part of the laser reflected by the β-BBO crystal could re-enter the laser cavity; however, when it was not normally incident, all the reflected fundamental lasers would go out of the cavity.

3.2.2. Analyses

To further understand the wavelength tuning, we did some simulations about the transmittances of the Lyot filter used in the experiment at different angles (the angle between the optical axis of the quartz plate and the incident plane) and wavelengths, and the relative phase-matching angles (0° corresponds to the normal incidence) of the β-BBO crystal corresponding to different wavelengths. The transmittances of the Lyot filter could be obtained through the Jones matrix[42]:

$$M_{\mathrm{b}} = \begin{pmatrix} \cos^2\alpha + \sin^2\alpha\exp(-i2\delta) & q\sin\alpha\cos\alpha\left[1-\exp(-i2\delta)\right] \\ q\sin\alpha\cos\alpha\left[1-\exp(-i2\delta)\right] & q^2\left[\sin^2\alpha+\cos^2\alpha\exp(-i2\delta)\right] \end{pmatrix},$$
(3)

where n is the refractive index (1.54 in the simulation) of the quartz, $q = 2n/\left(1+n^2\right)$, α is the angle between the incident plane and the plane defined by the optical axis of the quartz crystal and the refractive ray and -2δ is the phase retardation. By setting the transmission peak at 698 nm, a round trip transverse magnetic (TM) mode transmission curve is presented as a dashed line in Figure 6(a). By taking the influence of the β-BBO crystal on the tuning into consideration (the β-BBO crystal could be treated as a phase retarder because it is a uniaxial crystal with an AR coating around 698 nm), another simulation result is presented as a red line in Figure 6(a). As seen, the β-BBO crystal under the type-I phase-matching condition in our experiment could broaden the transmission peak and reduce the capability of wavelength selection. It could be one of the reasons why we could not obtain continuous tuning and could be improved by multiplying the quartz plates in the future. The phase-matching angle (type-I phase matching) could be calculated through the following equation[43]:

$$\sin^2\theta_{\mathrm{m}} = \frac{\left(n_\omega^{\mathrm{o}}\right)^{-2} - \left(n_{2\omega}^{\mathrm{o}}\right)^{-2}}{\left(n_{2\omega}^{\mathrm{e}}\right)^{-2} - \left(n_{2\omega}^{\mathrm{o}}\right)^{-2}},$$
(4)

where the refractive indexes (n) at different frequencies and polarization directions can be intuitively read by the superscripts and subscripts and θ_m is the phase-matching angle. The refractive indexes could be calculated through the Sellmeier equations from the following[44]:

$$n_o^2 = 2.7359 + \frac{0.01878}{\lambda^2 - 0.01822} - 0.01354\lambda^2,$$
$$n_e^2 = 2.3753 + \frac{0.01224}{\lambda^2 - 0.01667} - 0.01516\lambda^2, \qquad (5)$$

where λ is the laser wavelength. The simulation results are shown in Figure 6(b). As seen, the relative phase-matching angles required in the experiment were not very large (in $\pm 2°$). Thus, only slight tilting of the β-BBO crystal was needed in the experiment to achieve the wavelength tuning.

4. Conclusion

In this work, based on Pr³⁺:YLF and β-BBO crystals, we realize LD-pumped high-power (1.033 W) single-wavelength CW intracavity frequency-doubled UV lasers at 348.7 nm and discrete tunable CW UV lasers from 334.7 to 364.5 nm. The output powers of discretely tunable lasers are in the tens of milliwatts range, with the exception of the lasers at 348.7 and 360.3 nm (~500 mW). In addition, tuning theories are developed to explain the tuning mechanisms of mixing the Lyot filter and the β-BBO crystal. As far as we are aware, watt-level output power of the 348.7-nm laser is achieved for the first time, as well as discrete tunable UV lasers based on the Pr³⁺:YLF crystal. Compared with traditional high-power CW UV laser sources, the innovative approaches we proposed are expected to be simpler, less expensive and more compact competitors. For further works in the future, a laser cavity with fewer laser mode sensitivities to the thermal lensing effects can be designed to reduce the influences of the thermal lensing effects to obtain higher output power. Higher pump power, multiple quartz plates and the AR coating on the β-BBO crystal with higher quality can be applied to realize continuously tunable UV lasers.

Acknowledgements

Supplementary Materials

To view supplementary material for this article, please visit http://doi.org/10.1017/hpl.2022.32.

References

1. P. Fuerschbach and G. Eisler, Sci. Technol. Weld. Join. **7**, 241 (2002).
2. Z. Wang, J. Dirrenberger, P. Lapouge, and S. Dubent, Mater. Sci. Eng. A **831**, 142205 (2022).
3. A. Ogura, K. Yamasaki, D. Kosemura, S. Tanaka, I. Chiba, and R. Shimidzu, Jpn. J. Appl. Phys. **45**, 3007 (2006).
4. H. M. Shapiro and W. G. Telford, Curr. Protoc. Cytom. **49**, 1.9.1 (2009).
5. J. Georges, Appl. Spectrosc. **59**, 1103 (2005).
6. S. Davi, Lasers Surg. Med. **5**, 239 (1985).
7. H. Kitano, T. Matsui, K. Sato, N. Ushiyama, M. Yoshimura, Y. Mori, and T. Sasaki, Opt. Lett. **28**, 263 (2003).
8. S. Szatmári, Appl. Phys. B **58**, 211 (1994).
9. H. R. Lüthi, J. Appl. Phys. **48**, 664 (1977).
10. E. Armandillo and A. J. Kearsley, Appl. Phys. Lett. **41**, 611 (1982).
11. P. G. O'Shea and H. P. Freund, Science **292**, 1853 (2001).
12. A. K. Mohamed, A. Mustellier, J.-P. Faleni, and E. Rosencher, Opt. Lett. **27**, 1457 (2002).
13. A. Aadhi, N. A. Chaitanya, R. P. Singh, and G. K. Samanta, Opt. Lett. **39**, 3410 (2014).
14. J. M. Rodríguez-García, D. Pabœuf, and J. E. Hastie, IEEE J. Sel. Top. Quantum Electron. **23**, 5100608 (2017).
15. J. Pinto, G. Rosenblatt, L. Esterowitz, V. Castillo, and G. Quarles, Electron. Lett. **30**, 240 (1994).
16. N. Y. Joly, J. Nold, W. Chang, P. Hölzer, A. Nazarkin, G. K. L. Wong, F. Biancalana, and P. S. J. Russell, Phys. Rev. Lett. **106**, 203901 (2011).
17. A. Brenier and G. Boulon, J. Lumin. **86**, 125 (2000).
18. T. Gün, P. Metz, and G. Huber, Opt. Lett. **36**, 1002 (2011).
19. X. Lin, Q. Feng, X. Liu, S. Ji, B. Xiao, H. Xu, and Z. Cai, Opt. Lett. **47**, 3051 (2022).
20. S. Luo, X. Yan, Q. Cui, B. Xu, H. Xu, and Z. Cai, Opt. Commun. **380**, 357 (2016).
21. P. W. Metz, F. Reichert, F. Moglia, S. Müller, D.-T. Marzahl, C. Kränkel, and G. Huber, Opt. Lett. **39**, 3193 (2014).
22. X. Lin, Q. Feng, Y. Zhu, S. Ji, B. Xiao, H. Xu, W. Li, and Z. Cai, Opto-Electron. Adv. **4**, 21000601 (2021).
23. H. Tanaka, S. Fujita, and F. Kannari, Appl. Opt. **57**, 5923 (2018).
24. X. Liu, Z. Li, C. Shi, B. Xiao, R. Fang, Y. Xue, Q. Feng, X. Lin, Y. Zhu, G. Xu, H. Xu, and Z. Cai, Laser Phys. **32**, 025801 (2022).
25. M. Fibrich, J. Šulc, and H. Jelínková, Proc. SPIE **9726**, 97261E (2016).
26. X. Lin, M. Chen, Q. Feng, S. Ji, S. Cui, Y. Zhu, B. Xiao, W. Li, H. Xu, and Z. Cai, Opt. Laser Technol. **142**, 107273 (2021).
27. Z. Liu, Z. Cai, S. Huang, C. Zeng, Z. Meng, Y. Bu, Z. Luo, B. Xu, H. Xu, C. Ye, F. Stareki, P. Camy, and R. Moncorgé, J. Opt. Soc. Am. B **30**, 302 (2013).
28. Y. Ma, A. Vallés, J.-C. Tung, Y.-F. Chen, K. Miyamoto, and T. Omatsu, Opt. Express **27**, 18190 (2019).
29. X. Lin, Y. Zhu, S. Ji, W. Li, H. Xu, and Z. Cai, Opt. Laser Technol. **129**, 106281 (2020).
30. A. Richter, N. Pavel, E. Heumann, G. Huber, D. Parisi, A. Toncelli, M. Tonelli, A. Diening, and W. Seelert, Opt. Express **14**, 3282 (2006).
31. Y. Zhang, J. Zou, W. Zheng, K. Feng, B. Xu, and Z. Yu, Chin. Opt. Lett. **19**, 091406 (2021).
32. V. Ostroumov and W. Seelert, Proc. SPIE **6871**, 68711K (2008).
33. N. Niu, S. Pu, Q. Chen, Y. Wang, Y. Zhao, W. Wu, and Q. Zheng, Appl. Opt. **57**, 9798 (2018).
34. P. Zhu, C. Zhang, K. Zhu, Y. Ping, P. Song, X. Sun, F. Wang, and Y. Yao, Opt. Laser Technol. **100**, 75 (2018).
35. V. Ostroumov, W. Seelert, L. Hunziker, C. Ihli, A. Richter, E. Heumann, and G. Huber, Proc. SPIE **6451**, 645103 (2007).
36. A. S. Rao, K. Miamoto, and T. Omatsu, Opt. Express **28**, 37397 (2020).

37. Z. Liu, Z. Cai, B. Xu, C. Zeng, S. Huang, F. Wang, Y. Yan, and H. Xu, IEEE Photonics J. **5**, 1500905 (2013).
38. J. L. Adam, W. A. Sibley, and D. R. Gabbe, J. Lumin. **33**, 391 (1985).
39. D. N. Nikogosyan, Appl. Phys. Solids Surf. **52**, 359 (1991).
40. R. Smith, IEEE J. Quantum Electron. **6**, 215 (1970).
41. A. Agnesi, A. Guandalini, and G. Reali, J. Opt. Soc. Am. A **19**, 1078 (2002).
42. S. Zhu, Appl. Opt. **29**, 410 (1990).
43. R. W. Boyd, *Nonlinear Optics* (Elsevier, San Diego, 2019).
44. K. Kato, IEEE J. Quantum Electron. **22**, 1013 (1986).